Scientific Research Publishing

Open Journal of Energy Efficiency, 2026, 15(3), 111-138
https://www.scirp.org/journal/ojee
ISSN Online: 2169-2645
ISSN Print: 2169-2637

Experimental Research on the Co-Combustion Characteristics of High-Calorific Bituminous Coal and Anthracite

Zhu Cui[1], Yangyang Ma[1], Jiahui Zhao[2], Dazhuang Liu[2], Xin Zhang[3*]

[1]Hubei Chibi Electric Power Co., Ltd., Chibi, China
[2]Beijing Yelian Technology Co., Ltd., Beijing, China
[3]School of Energy Science and Engineering, Harbin Institute of Technology, Harbin, China
Email: *2057769574@qq.com

How to cite this paper: Cui, Z., Ma, Y.Y., Zhao, J.H., Liu, D.Z. and Zhang, X. (2026) Experimental Research on the Co-Combustion Characteristics of High-Calorific Bituminous Coal and Anthracite. *Open Journal of Energy Efficiency*, **15**, 111-138.
https://doi.org/10.4236/ojee.2026.153006

Received: August 20, 2026
Accepted: September 21, 2026
Published: September 24, 2026

Abstract

Understanding how coals of different ranks interact during combustion requires linking macroscopic combustion behavior with reaction kinetics, mineral transformations, and microstructural evolution. Here, high-calorific-value bituminous coal (GY), anthracite (WY), and their 1:1 blend (GYW) were examined by thermogravimetric/derivative thermogravimetric analysis (TG-DTG), a mass-weighted non-additivity assessment, model-free isoconversional kinetics (DAEM, FWO, and Starink), X-ray diffraction (XRD), and scanning electron microscopy coupled with energy-dispersive X-ray spectroscopy (SEM-EDS). GY ignited earlier than WY (T_i = 294.12˚C versus 412.95˚C), consistent with its higher volatile-matter content. GYW showed small, sign-changing departures from the mass-weighted reference. With $\Delta w = TG_{exp} - TG_{cal}$, positive Δw denotes greater retained mass (apparent inhibition), whereas negative Δw denotes lower retained mass (apparent promotion); at 10˚C/min, the extrema were +0.981% near 590˚C and −0.739% near 528˚C. Because each condition was retained as a duplicate (n = 2) and the observed deviations (0.22% - 1.65% across the reported conditions) were within the <2% curve-reproducibility screening criterion, they are treated as descriptive non-additivity rather than statistically resolved synergy. At the same conversion, the apparent activation-energy profile of GYW generally lay between those of GY and WY and did not demonstrate a systematic lowering of the WY barrier. XRD and SEM directly support differences in mineral assemblage, surface coverage, and pore accessibility; thermal coupling, reactive-intermediate transfer, pore evolution, and Ca/AAEM-mediated catalysis remain plausible, literature-supported interpretations rather than demonstrated causal pathways. The EDS compositions are local semi-quantitative surface measurements and are

not bulk residual-carbon contents. This evidence-bounded interpretation provides a more internally consistent description of GY/WY co-combustion.

Keywords

Coal Co-Combustion, Thermogravimetric Analysis, Non-Additive TG Deviation, Isoconversional Kinetics, XRD, SEM-EDS, Mineral Transformation, Ash Evolution

1. Introduction

Coal remains a major component of the global energy mix, making improvements in its combustion efficiency and environmental performance an enduring challenge in the energy sector [1] [2]. China has abundant coal resources spanning a wide range of ranks, including anthracite, whose high degree of aromatic condensation, low volatile-matter content, and high ignition temperature can lead to difficult ignition, incomplete burnout, and elevated NO_x emissions when it is burned alone [3] [4]. Co-combustion offers a practical route to mitigate these limitations by blending a highly reactive coal with a less reactive one so that their combustion characteristics become complementary. This strategy has therefore been widely considered for utility and industrial boilers because it can improve ignition and burnout while reducing pollutant formation [5] [6]. Previous studies, including those of Zhang *et al.* [7] and Yang *et al.* [8], have shown that adding bituminous coal to anthracite can improve the overall combustion performance of the blend and reduce emissions such as CO_x and NO_x.

Most previous studies have evaluated coal-blend combustion using TG-DTG analysis together with kinetic calculations to quantify changes in reactivity and reaction barriers. Tong *et al.* [9], for example, demonstrated positive interactions among three blended-coal formulations and showed that appropriate blending could reduce the apparent activation energy; they also noted that the conventional Coats-Redfern method may not fully describe the complex kinetics of multicomponent coal blends. Wang *et al.* [10] likewise reported that the TG/DTG profiles of blended coals did not follow simple linear superposition, despite lying broadly between those of the parent coals. Their isoconversional analysis further confirmed interactions between the individual components. These studies establish that non-additive behavior is common in blended-coal combustion, but they mainly describe the phenomenon at the macroscopic and kinetic levels.

A remaining challenge is to explain why such non-additive behavior emerges. Coal co-combustion simultaneously involves volatile release, char oxidation, heat and mass transfer, mineral transformation, and ash-structure evolution, and these processes operate across different spatial and temporal scales [11] [12]. Macroscopic combustion indices alone therefore cannot identify how mineral composition and microstructure contribute to the observed deviations [13] [14]. Con-

versely, XRD and SEM are often used as stand-alone characterization tools, with limited integration with combustion-stage evolution, changes in apparent activation energy, or temperature-dependent departures from additive behavior. This gap is particularly important for blends of different coal ranks, where differences in aromatic structure, pore accessibility, and mineral assemblage may be associated with oxygen transport, reactive-intermediate transfer, and char oxidation but do not, by themselves, prove those causal pathways.

To address this gap, the present study combines TG-DTG analysis, a mass-weighted non-additivity assessment, model-free isoconversional kinetics, and multiscale XRD/SEM-EDS characterization to construct an evidence chain linking mineral composition and microstructure to reaction kinetics and macroscopic combustion behavior. Specifically, the study aims to 1) identify measured structural and mineralogical differences associated with the contrasting combustion behavior of GY and WY; 2) determine the temperature-dependent TG deviations of their 1:1 blend and compare the parent and blend activation-energy profiles at the same conversion; and 3) distinguish directly observed mineral/microstructural evidence from proposed explanations involving heat transfer, reactive intermediates, pore evolution, and mineral-mediated effects. The analysis is descriptive and does not claim statistical resolution of deviations that fall within the experimental reproducibility criterion.

2. Materials and Methods

2.1. Experimental Materials and Characteristics

Table 1. Basic properties of the experimental coal samples.

Test	GY	WY
Proximate analysis (wt.%)		
Moisture content (M_{ad})	3.62	3.57
Ash content (A_{ad})	15.41	18.48
Volatile matter (V_{ad})	28.84	7.44
Fixed carbon (FC_{ad})	52.13	70.51
HHV (MJ/Kg)	25.88	26.17
Ultimate analysis (wt.%)		
C	68.71	73.04
H	4.07	2.55
N	1.05	0.99
S	0.89	0.67
O	5.28	5.45

The high-calorific-value bituminous coal (GY) and anthracite (WY) used in this study were obtained from the industrial coal supply of Hubei Chibi Electric Power Co., Ltd. Before testing, both raw coals were dried at 105˚C for 8 h, coarsely

crushed, finely ground, and sieved to obtain the 100 - 200 mesh fraction. Their proximate and ultimate analyses are summarized in Table 1. The blended sample, denoted GYW, was prepared by thoroughly mixing GY and WY at a mass ratio of 1:1.

2.2. Experimental Methods

2.2.1. Thermogravimetric Analysis Equipment

Combustion tests of the pretreated high-calorific-value bituminous coal (GY), anthracite (WY), and their 1:1 blend (GYW) were performed using a thermogravimetric analyzer (TGA 550, TA Instruments, USA), with the experimental setup shown schematically in Figure 1. Before formal tests, empty alumina crucibles were pre-calcined at 1000˚C to remove residual impurities, and blank runs under identical temperature programs were conducted for baseline correction of buoyancy and instrumental drift. For all formal combustion tests, approximately 9.8 ± 0.2 mg of sample was spread uniformly in the alumina crucible to limit heat- and mass-transfer gradients within the bed. The sample was heated from 30 to 1000˚C at 5˚C, 10˚C, or 20˚C/min. High-purity air (99.99%) was supplied at 60 mL/min to maintain an oxidizing atmosphere. Each condition was measured in duplicate, and two curves satisfying a maximum pointwise relative mass difference below 2% were retained (n = 2 per condition). Reported TG curves and derived point estimates were obtained from the retained duplicate measurements. Because n = 2 does not support stable estimates of SD or confidence intervals, no p values or inferential claims are reported; TG deviations, characteristic temperatures, and kinetic parameters are interpreted descriptively.

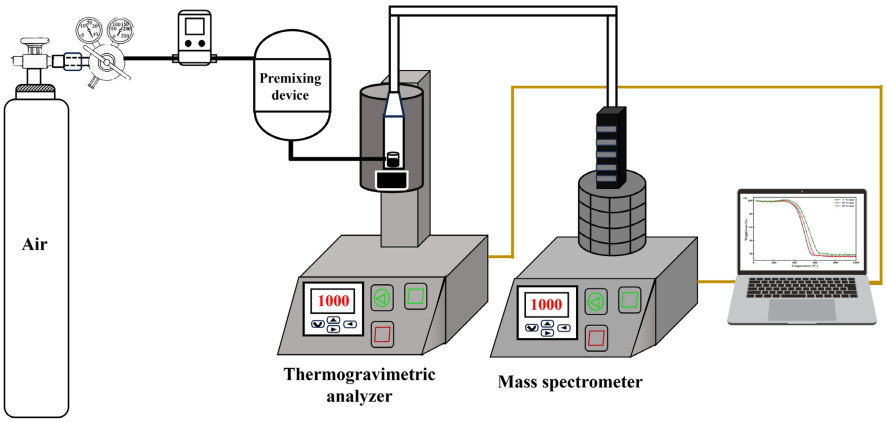

Figure 1. Schematic diagram of a thermogravimetric analysis system.

2.2.2. Combustion Performance Evaluation

To quantitatively evaluate the combustion characteristics of the tested single and blended coal samples under different heating rates, two dimensionless indices, namely the combustion completeness index (C) and the comprehensive combustion performance index (S), are introduced in this study. These two indices are adopted to systematically quantify the burnout degree and overall reaction per-

formance of coal samples during the non-isothermal combustion process, and their detailed calculation formulations are defined in Equations (1)-(3) [15].

$$DTG_{\text{mean}} = \frac{\beta\left(TG_i - TG_b\right)}{T_b - T_i} \tag{1}$$

$$C = \frac{DTG_{\max}}{T_i^2} \tag{2}$$

$$S = \frac{DTG_{\max} DTG_{\text{mean}}}{T_i^2 T_b} \tag{3}$$

where T_i is the ignition temperature of the coal sample, in K; T_b is the burnout temperature, defined as the temperature at which 98 wt.% of the total mass loss is consumed, in K; TG_i and TG_b are the residual mass fractions at T_i and T_b respectively, in %; $DTG_{\max}$ and DTG_{mean} are the maximum mass loss rate and the average mass loss rate during the main combustion stage, respectively, in %/s.

2.2.3. Kinetic Analysis Method

Coal combustion is a highly intricate heterogeneous reaction system consisting of a series of parallel, competitive, and consecutive sub-reactions, whose overall reaction kinetics and apparent chemical dynamics are fundamentally governed by the apparent activation energy (E_α) at different conversion stages [16].

The kinetic equation describing the reaction process is given by Equation (4) [17]:

$$\frac{d\alpha}{dt} = k(T) f(\alpha) \tag{4}$$

In this equation, $f(\alpha)$ is the reaction-model function used to describe the overall coal-combustion conversion, and $k(T)$ is the temperature-dependent rate constant defined by the Arrhenius law. R is the universal gas constant (8.314 $\times 10^{-3}$ kJ/(mol·K)).

Introducing β ($\beta = dT/dt$) and letting the transfer function be $f(\alpha) = (1-\alpha)$, we obtain the following equation:

$$\frac{d\alpha}{dt} = \left(\frac{A}{\beta}\right)\exp\left(\frac{-E_\alpha}{RT}\right)(1-\alpha) \tag{5}$$

Under the initial conditions $T = T_0$ and $\alpha = 0$, and when $RT^2/E_\alpha \ll 1$, Equation (6) is obtained.

$$g(\alpha) = \int_0^\alpha \frac{d\alpha}{(1-\alpha)} = \left(\frac{ART^2}{\beta E}\right)\exp\left(\frac{-E_\alpha}{RT}\right) \tag{6}$$

As recommended by the Kinetics Committee of the International Confederation for Thermal Analysis and Calorimetry (ICTAC), kinetic analysis based on multiple heating rate datasets via model-free methods can produce more robust and reliable kinetic parameters than those derived from a single heating rate program [18] [19]. Accordingly, the constant conversion rate principle was adopted in this study, and three typical model-free kinetic methods, *i.e.*, the DAEM, Flynn-

Wall-Ozawa (FWO) and Starink method, were jointly applied to perform the kinetic calculation. The core analytical equations corresponding to these three models are summarized in Table 2.

Table 2. Computational methods for determining kinetic parameters.

Model fitting kinetics analysis			
Method	Kinetic equation	Plot	Slope
DAEM [20]	$\ln\left[\frac{\beta_i}{T_\alpha^2}\right]=\ln\left[\frac{AR}{E_\alpha}\right]+0.6075-\left[\frac{E_\alpha}{RT_\alpha}\right]$	$\ln\left[\frac{\beta_i}{T_\alpha^2}\right]Vs\frac{1}{T}$	$-E_\alpha/R$
FWO [21]	$\ln\beta_i=\ln\left[\frac{AE_\alpha}{Rg(\alpha)}\right]-5.3305-1.052\left[\frac{E_\alpha}{RT_\alpha}\right]$	$\ln\beta_i Vs\frac{1}{T}$	$-E_\alpha/R$
Starink [22]	$\ln\left[\frac{\beta_i}{T_\alpha^{1.92}}\right]=Const.-1.0008\left[\frac{E_\alpha}{RT_\alpha}\right]$	$\ln\left[\frac{\beta_i}{T_\alpha^{1.92}}\right]Vs\frac{1}{T}$	$-E_\alpha/R$

2.3. Sample Characterization

2.3.1. X-Ray Diffraction (XRD)

X-ray diffraction (XRD) was used to characterize the mineral assemblages of GY, WY, and GYW and to track the evolution of crystalline inorganic phases after combustion. Samples were thoroughly ground and sieved before being evenly mounted for analysis. Measurements were performed using Cu Kα radiation (λ = 0.15406 nm) over 5˚ - 90˚ (2θ), with a step size of 0.02˚ and a scanning rate of 5˚/min. Mineral phases, including quartz, kaolinite, illite, calcite, and dolomite, were identified from peak position, shape, and relative intensity by comparison with the standard PDF database. The corresponding combustion ashes were analyzed under the same framework to connect Ca^{2-}, Si^{4-}, Al^{3-}, and Fe-bearing phase transformations with the observed combustion and ash-evolution behavior.

2.3.2. Scanning Electron Microscopy-Energy-Dispersive X-Ray Spectroscopy (SEM-EDS)

Scanning electron microscopy coupled with energy-dispersive X-ray spectroscopy (SEM-EDS) was used to examine surface morphology, pore accessibility, and elemental distribution in the raw coals and combustion ashes. Samples were dried, mounted on conductive adhesive, and surface-coated before observation. SEM imaging was performed at an accelerating voltage of 15 kV over multiple magnifications to characterize particle morphology, cracks, and pores. EDS was used for local, semi-quantitative elemental analysis and spatial mapping of C, O, Si, Al, Ca, Fe, S, and other detected elements in representative fields. Because replicate fields and a bulk carbon assay were not available, the EDS values are not treated as bulk composition or bulk residual-carbon fractions.

The SEM-EDS observations were interpreted together with the TG-DTG profiles, kinetic parameters, and XRD results. This cross-comparison was used to assess how coal-rank-dependent microstructure, oxygen-transport pathways, and

mineral redistribution were associated with the co-combustion behavior, rather than treating the individual characterization techniques as independent evidence.

3. Results and Discussion

3.1. Combustion Performance

Because coal combustion involves overlapping devolatilization, oxidation, and mineral-transformation processes, continuous mass-loss measurements are particularly useful for resolving their temperature dependence. The TG-DTG results were therefore used as the primary macroscopic framework, to which the kinetic and microstructural evidence was subsequently linked.

3.1.1. Thermogravimetric Analysis

The combustion characteristic curves for GY, WY, and GYW at a heating rate of 10˚C/min are shown in **Figure 2**. For descriptive purposes, the overall mass-loss process is divided into three temperature regions.

The first region corresponds mainly to moisture removal and weak low-temperature oxidation. At T < 150˚C, all three samples show only minor mass loss (approximately 1.2% cumulatively), and their DTG curves remain close to the baseline. Net mass gains are subsequently observed for GY over approximately 150˚C - 295˚C and for WY over approximately 150˚C - 410˚C; the GY gain reaches about 1.3%. These increases suggest that oxygen uptake may exceed concurrent mass release before rapid combustion begins. Differences in volatile content, organic functionality, aromatic condensation, mineral coverage, and pore accessibility provide plausible explanations for the different temperature windows. However, peroxide intermediates, individual functional groups, and specific radical sites were not measured in this study; their roles are therefore treated as literature-based interpretations rather than direct observations.

The second region contains the principal combustion of released volatiles and fixed carbon. GY shows a shoulder-like two-part DTG feature: mass loss over approximately 295˚C - 380˚C is associated mainly with early volatile release and oxidation, followed by a broader, more intense event over approximately 380˚C - 630˚C. WY enters its main mass-loss region later, near 400˚C, and shows a broader single event with little early volatile contribution. The observed peak mass-loss rates are 7.21%/min for GY and 8.81%/min for WY at 10˚C/min. These differences are consistent with the higher volatile content of GY and the lower volatile content and more condensed carbon structure of WY [23]. The assignments to peroxide decomposition, aromatic-ring opening, and internal oxygen-diffusion control remain proposed molecular-level explanations because the present measurements do not directly resolve those processes.

The third region, approximately 630˚C - 800˚C, is characterized by a much smaller mass-loss rate as the TG curves approach a plateau. The remaining mass change is consistent with carbonate decomposition (for example, $CaCO_3 \rightarrow CaO + CO_2$) and solid-state transformations of aluminosilicate and sulfate phases. A TG plat-

eau indicates that the major combustible mass loss is largely complete, but it does not demonstrate the total absence of residual carbon. The local C signals detected by EDS in representative ash fields (Section 3.4.2) may include residual carbon and/or mounting and sampling contributions; because EDS is local and semi-quantitative, those values cannot be used to quantify bulk burnout. Accordingly, the earlier statement that all organic matter was completely consumed has been removed.

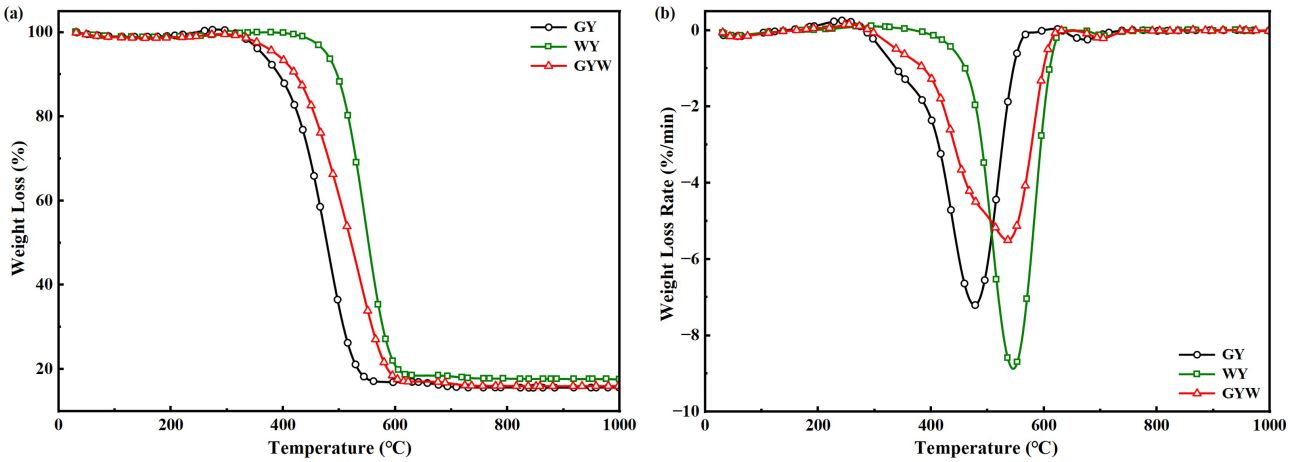

Figure 2. Combustion characteristic curves of GY, WY, and GYW at a heating rate of 10˚C/min, (a) TG, (b) DTG.

In summary, GY and WY occupy different combustion-temperature windows that are consistent with their contrasting volatile and fixed-carbon contents. GYW exhibits intermediate ignition and burnout temperatures and a broadened DTG profile, showing overlap of the two parent-coal processes. The earlier ignition of GYW relative to WY is expected from the presence of the more readily ignited GY fraction; it does not by itself demonstrate that blending lowers the intrinsic kinetic barrier of WY. Because the measured TG departures from the mass-weighted reference are small and fall within the stated reproducibility screen, the curves are discussed as descriptive non-additivity rather than proof of a statistically significant synergistic enhancement.

3.1.2. The Effect of Different Heating Rates

The heating rate (β) is one of the most critical process parameters that significantly affect the non-isothermal combustion reaction pathway, the devolatilization kinetics of coal matrix, and the final distribution of gas and solid combustion products. To systematically clarify the influence of heating rate on the overall combustion performance of the GY, WY and GYW, a series of thermogravimetric tests were performed at three heating rates of 5, 10 and 20˚C/min. The corresponding TG and DTG combustion characteristic profiles of each sample under different heating rate conditions are comparatively illustrated in **Figure 3**.

As observed from the TG/DTG profiles, the overall combustion sequence of all three samples remains similar across the three heating rates. Increasing the heating rate shifts the characteristic regions toward higher measured temperatures,

indicating thermal lag under non-isothermal conditions. Faster programmed heating can increase temperature gradients and reduce the time available for intraparticle heat and mass transport, so devolatilization and oxidation are registered at higher furnace temperatures. The shift is more pronounced for WY, consistent with its low volatile content and limited pore accessibility [24]. These observations concern combustion in flowing air; references to an inert or purely pyrolytic atmosphere have been removed.

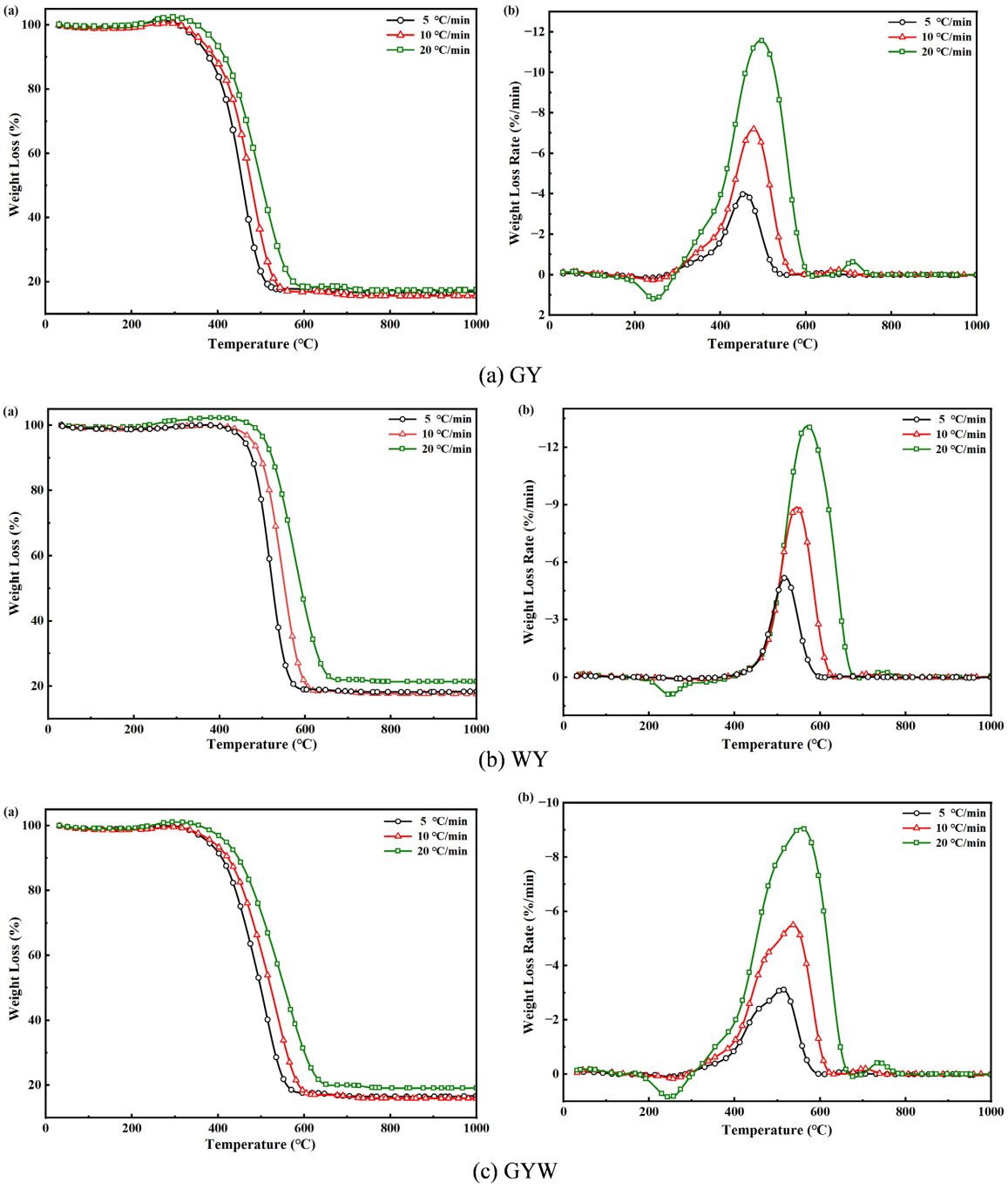

(a) GY

(b) WY

(c) GYW

Figure 3. Combustion characteristic curves of GY, WY, and GYW at different heating rates.

The main DTG region also broadens toward higher temperature as the heating rate increases. The maximum mass-loss rate increases from 4.02% to 11.57%/min for GY, from 5.11% to 12.78%/min for WY, and from 3.21% to 9.30%/min for GYW. This increase is consistent with temporal compression and greater overlap of devolatilization and char oxidation at faster programmed heating. A higher peak rate should not, however, be interpreted by itself as greater combustion completeness or as proof of stronger inter-coal synergy.

3.1.3. Combustion Performance Analysis

Table 3. Combustion performance parameters of various coal samples at different heating rates.

β (˚C/min)	Sample	T_i (˚C)	T_b (˚C)	DTG_{max} (%/s)	DTG_{mean} ($\times10^{-2}$ %/s)	C ($\times10^{-7}$)	S ($\times10^{-8}$)
5	GY	284.05	523.67	0.067	2.841	8.294	0.450
	WY	405.04	584.11	0.085	3.446	5.187	0.303
	GYW	286.41	563.80	0.053	2.554	6.522	0.296
10	GY	294.12	556.20	0.120	5.405	1.324	1.31
	WY	412.95	616.87	0.147	6.223	0.841	0.843
	GYW	299.17	597.05	0.096	4.820	1.066	0.861
20	GY	312.24	586.35	0.193	9.761	2.030	3.379
	WY	464.026	659.27	0.213	10.745	1.131	1.827
	GYW	311.92	634.84	0.155	8.467	1.635	2.180

Table 3 summarizes point estimates of the combustion-performance parameters obtained from the retained duplicate TG curves (n = 2 per condition). At 10˚C/min, WY has higher ignition and burnout temperatures (T_i = 412.95˚C and T_b = 616.87˚C) than GY (T_i = 294.12˚C and T_b = 556.20˚C), consistent with lower low-temperature reactivity. Contrary to the previous statement, C and S do not both increase monotonically with heating rate. The C values ($\times10^{-7}$) change as 8.294 → 1.324 → 2.030 for GY, 5.187 → 0.841 → 1.131 for WY, and 6.522 → 1.066 → 1.635 for GYW as the rate increases from 5˚C to 10˚C to 20˚C/min; C therefore decreases sharply and then only partially recovers. By contrast, S ($\times10^{-8}$) increases monotonically: 0.450 → 1.310 → 3.379 for GY, 0.303 → 0.843 → 1.827 for WY, and 0.296 → 0.861 → 2.180 for GYW. Thus, faster heating raises the rate-dependent S index while producing a non-monotonic response in C, and it cannot be described simply as improving all aspects of combustion. Because only duplicate runs were retained, SD/CI and p values are not reported and these comparisons are descriptive.

3.2. TG-Based Non-Additivity Assessment

To quantify departures of GYW from a mass-weighted additive reference during combustion, a calculated TG curve was compared with the experimental blend curve. The reference curve was obtained from the TG profiles of GY and WY meas-

ured under the same oxidizing combustion conditions, using Equation (7) [15].

$$TG_{cal} = x_1 TG_{GY} + x_2 TG_{WY} \quad (7)$$

here, TG_{WY} and TG_{GY} are the experimental TG curves of WY and GY, respectively; x_1 and x_2 are their mass fractions in the blend; and TG_{cal} is the mass-weighted additive reference for GYW.

The deviation between the experimental blend curve and the mass-weighted reference is defined by Equation (8).

$$\Delta w = TG_{exp} - TG_{cal} \quad (8)$$

where TG_{exp} is the experimental TG curve of GYW. A positive Δw means that the experimental blend retains more mass than the additive reference at the same temperature and is therefore labeled apparent combustion inhibition (or delayed conversion). A negative Δw means that the blend retains less mass than the reference and is labeled apparent combustion promotion (or accelerated conversion). The sign of Δw alone does not establish statistical significance or a molecular mechanism.

Figure 4 shows small, sign-changing deviations of GYW from the mass-weighted reference. At 10˚C/min, the positive-negative-positive Δw sequence corresponds to apparent inhibition-promotion-inhibition, not positive-negative-positive enhancement. The most negative deviation, −0.739% near 528˚C, represents the largest apparent promotion, whereas the +0.981% deviation near 590˚C and the approximately +0.70% late-burnout deviation represent greater retained mass and therefore apparent inhibition. These deviations are evidence of non-additive curve shape; however, their magnitudes are below the <2% reproducibility screening criterion used for the retained duplicate curves. They cannot therefore be distinguished from experimental variability as statistically resolved synergy with the available n = 2 dataset.

The evidence and proposed mechanisms are distinguished as follows. TG-DTG directly shows temporal overlap and sign-changing deviations from the additive curve; XRD directly identifies the crystalline mineral assemblages and the absence of a new dominant bulk phase; SEM directly shows differences in cracks, pores, and mineral coverage; and EDS provides local elemental associations. In contrast, localized heat transfer from GY to WY, radical attack by H·/OH·, newly generated transport pathways, and catalytic action of Ca- or other AAEM-bearing species were not measured independently. These processes remain plausible hypotheses, supported by prior literature [25]-[27], for the observed stage dependence rather than proven causal pathways in the present experiments.

As the heating rate increases from 5 to 20˚C/min, the combustion curves shift toward higher temperatures because of thermal lag. In **Figure 4(b)**, the maximum positive Δw rises from 0.81% to 1.65%; under the corrected sign convention, this is an increase in the maximum apparent inhibition, not promotion. The positive late-burnout deviation decreases from 1.01% to 0.22%, indicating weaker apparent inhibition in that region. All of these deviations remain within the <2% repro-

ducibility screen and are therefore reported descriptively. Faster heating, shortened reaction time, volatile/char overlap, local heat exchange, radical transfer, and pore evolution may contribute to the changing curve shape, but local temperature, radical concentrations, and pathway-specific rates were not measured. These explanations are consequently presented as hypotheses rather than demonstrated mechanisms.

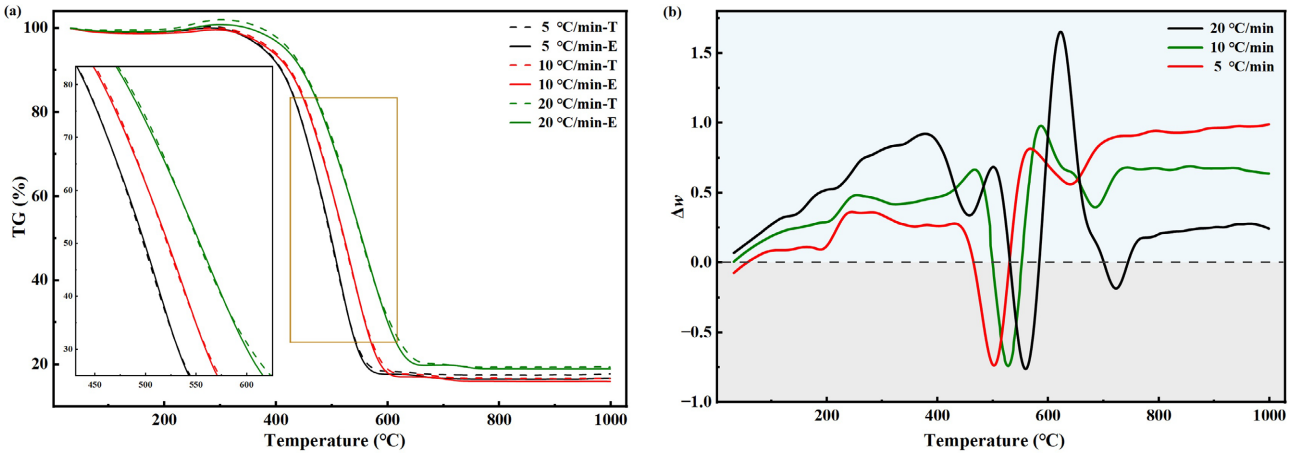

Figure 4. TG curves and TG-derived non-additive deviations for GY/WY blended combustion at different heating rates. Positive Δw denotes greater retained mass (apparent inhibition), whereas negative Δw denotes lower retained mass (apparent promotion).

3.3. Kinetic Analysis

The combustion processes of GY, WY, and GYW are not governed by a single reaction pathway but rather constitute a complex reaction network comprising parallel, competitive, and sequential reactions. The overall reaction behavior is controlled by multiple kinetic parameters, among which the apparent activation energy (E_α) is one of the most critical kinetic indicators. According to reaction kinetics theory, activation energy represents the minimum energy barrier that the reactants must overcome to transform from the ground state to the activated state. It directly governs the temperature sensitivity of the reaction rate, with a higher E_α indicating a more difficult reaction to initiate.

Table 4. R^2 values of fitted lines obtained using three model-free methods for calculating activation energy.

Sample	DAEM	FWO	Starink
GY	0.998	0.997	0.995
WY	0.989	0.992	0.987
GYW	0.982	0.987	0.990

For GY, WY, and GYW, isoconversional regressions were fitted at each conversion using data from the three heating rates. Table 4 and Figure 5 summarize the resulting fits. The coefficients of determination range from 0.982 to 1.000, sup-

porting the numerical linearity required by the three selected methods over the analyzed range. High R^2 values do not demonstrate that the three samples share an identical intrinsic reaction mechanism; they indicate only that the corresponding isoconversional regressions are well fitted [28].

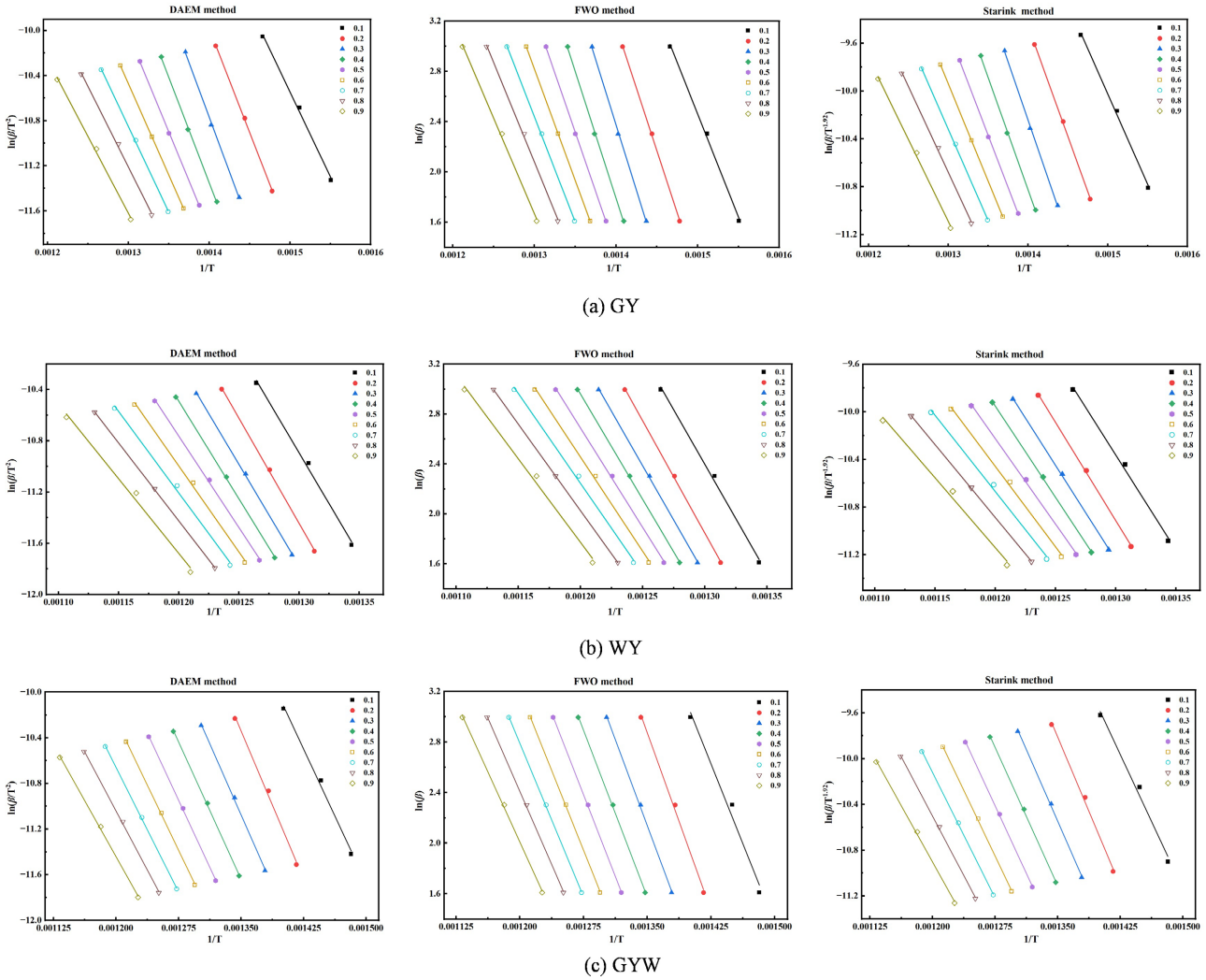

(a) GY

(b) WY

(c) GYW

Figure 5. Determination of the E_α values for GY, WY, and GYW using three model-free linear fitting methods.

Figure 6 presents the conversion-dependent apparent activation energies (E_α) obtained using DAEM, FWO, and Starink. The three methods give similar profile shapes, while FWO produces systematically higher values than DAEM and Starink, consistent with method-dependent approximations reported in the literature [29] [30]. The average E_α reported for GYW is approximately 128 kJ/mol. Any spread shown or quoted across the three methods reflects method-to-method dispersion, not replicate SD, a confidence interval, or experimental uncertainty. Because the kinetic calculation uses the retained duplicate TG curves at each heating rate and n = 2 is insufficient for stable inferential estimates, the kinetic comparisons below are descriptive.

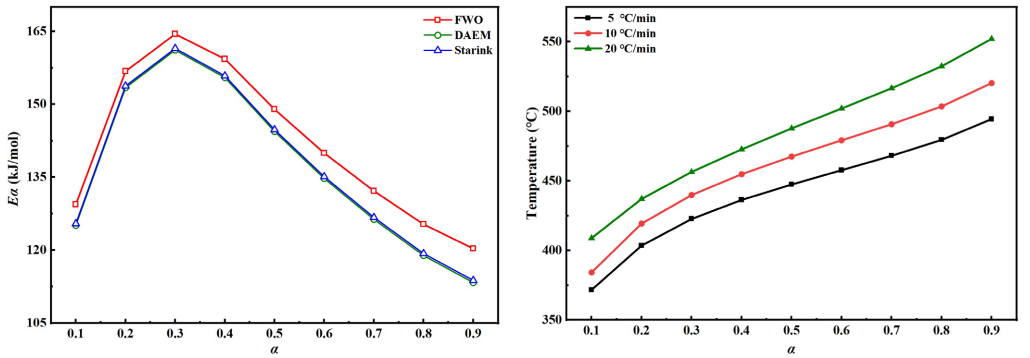

(a) GY

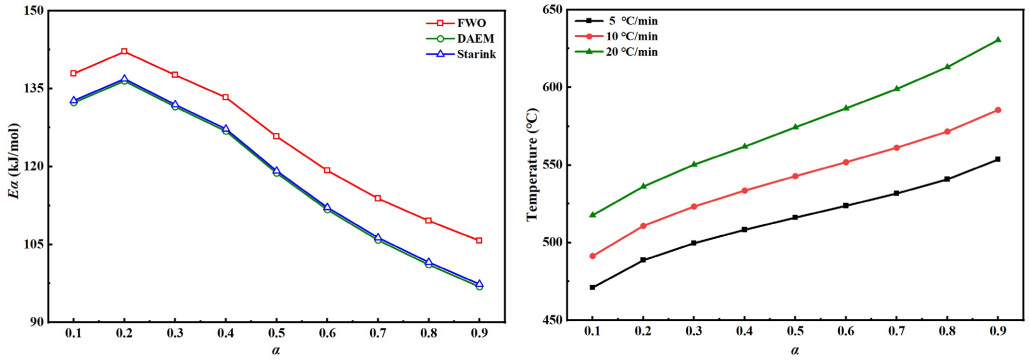

(b) WY

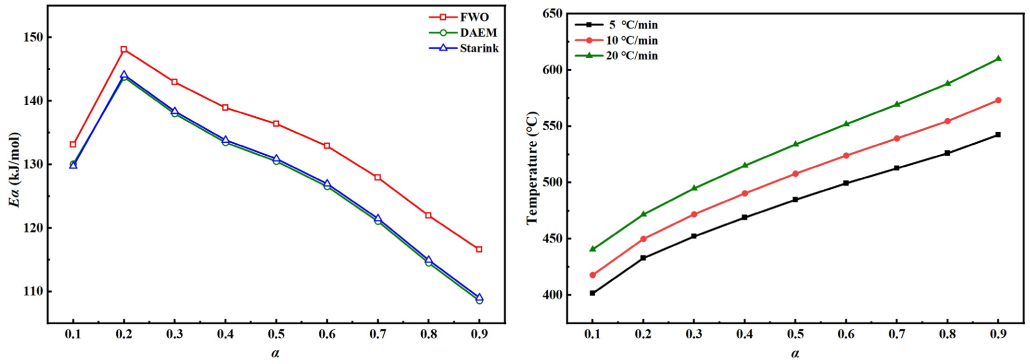

(c) GYW

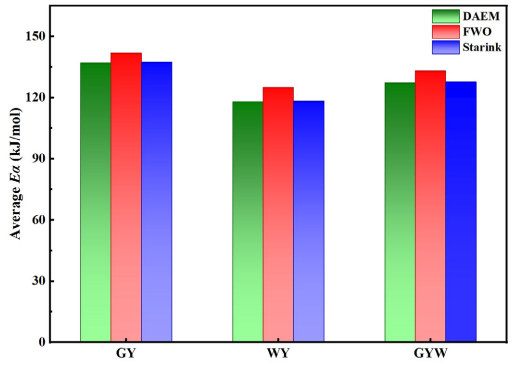

(d) Average

Figure 6. The relationship between E_α and α for GY, WY, and GYW, as well as the curves showing the relationship between α and temperature.

The variation of E_α exhibits a strong intrinsic correlation with the characteristic profiles of TG and DTG curves. A targeted correlation analysis integrating the E_α-α evolution diagrams in Figures 6(a)-(c) with the corresponding thermogravimetric curves reveals that the evolution pattern of E_α with α presents remarkable discrepancies among different coal samples.

For GY, E_α rises early and reaches approximately 162.14 kJ/mol near $\alpha = 0.3$, followed by a gradual decline to 113.35 kJ/mol near $\alpha = 0.9$. The position of the peak overlaps the major volatile-release/oxidation region of the TG-DTG curves. This correspondence is consistent with changing contributions from volatile oxidation and char oxidation as conversion proceeds. Explanations involving sequential release of light and heavy components and pore generation are plausible, but these individual pathways were not measured separately.

WY reaches a local E_α peak of approximately 136.15 kJ/mol near $\alpha = 0.2$ and then declines to 96.85 kJ/mol near $\alpha = 0.9$. GYW reaches approximately 143.57 kJ/mol near $\alpha = 0.2$ and generally lies between the GY and WY profiles when compared at the same conversion. Relative to the simple parent-coal mean, the position of the GYW curve is conversion-dependent rather than uniformly lower. In particular, GYW is not systematically below WY; the present kinetic results therefore do not demonstrate that blending lowers the intrinsic WY activation-energy barrier or directly promotes WY oxidation. The lower ignition temperature of GYW than WY can be explained by the presence and earlier combustion of GY. Heat transfer, evolving pore access, AAEM-mediated catalysis, and radical transfer may influence the blend profile, but these remain proposed mechanisms because they were not isolated by the measurements.

3.4. Characterization of Coal and Ash Samples

3.4.1. XRD Analysis

1) Raw coal samples

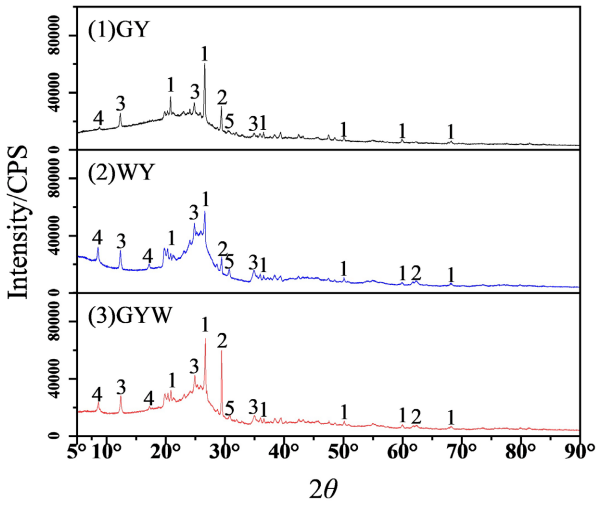

Figure 7. XRD patterns of the representative raw coal samples (1-quartz; 2-calcite; 3-kaolinite; 4-illite; 5-dolomite).

Figure 7 shows the XRD patterns of the raw coal samples. Quartz is the dominant crystalline phase in all three samples, with a strong (101) reflection at $2\theta =$ 26.6˚ and secondary reflections near 20.8˚, 36.5˚, and 50.1˚. Kaolinite and illite are also identified: the peaks at 8.8˚ and 24.8˚ correspond to kaolinite, while those near 19.8˚ and 35.0˚ are characteristic of illite. The relative abundance of clay-mineral reflections follows WY > GYW > GY, consistent with the higher ash content and Si-Al-rich character of WY. By contrast, GY exhibits a stronger calcite (104) reflection at 29.4˚, indicating a greater abundance of Ca-bearing carbonate minerals. The GYW pattern is intermediate, as expected for a 1:1 physical blend.

These mineralogical differences may be associated with part of the rank-dependent combustion behavior, but their effects are temperature-dependent and were not isolated experimentally. Dehydroxylation of kaolinite and illite is endothermic, and SEM shows platy mineral coverage on WY; together, these observations are compatible with restricted oxygen access and delayed oxidation [31] [32]. They do not quantify a transport resistance or prove that the minerals caused the measured ignition shift. XRD therefore supplies mineralogical context rather than an independent causal test.

The greater calcite abundance in GY may be relevant mainly at elevated temperature. Calcite decomposes at approximately 600˚C - 800˚C to form CaO and CO_2, linking it more directly to late char oxidation and ash evolution than to the initial ignition of GY. Literature indicates that CaO can provide basic surface sites and modify heterogeneous char-oxidation pathways [33], whereas calcite decomposition is endothermic and released CO_2 can locally dilute oxygen. These competing effects were not measured separately here. The early ignition of GY is therefore attributed primarily to its higher volatile content, while any Ca-mediated contribution is retained as a proposed high-temperature mechanism.

No additional independent diffraction peaks are observed for GYW, and all major peak positions can be traced to the two parent coals. This result indicates that blending does not generate a new dominant bulk crystalline mineral phase in the analyzed samples. Nevertheless, spatial proximity among Ca-, alkali-, and clay-bearing particles could still alter the local chemical environment. The positive Δw near 590˚C denotes apparent inhibition under Equation (8), not enhanced conversion. Its coincidence with a mineral-transformation temperature region is compatible with a mineral contribution, but TG and XRD do not quantify or isolate that contribution, and the deviation remains within the experimental reproducibility screen.

Overall, the XRD results distinguish thermally stable quartz, clay-mineral transformations, and Ca-bearing phases in the analyzed samples. GYW combines the parent mineral assemblages without a new dominant crystalline phase. These measurements establish phase presence and transformation but do not establish that mineral redistribution governs the small TG deviations; any mineral-mediated contribution remains a proposed, temperature-dependent interpretation.

2) Combustion ash samples

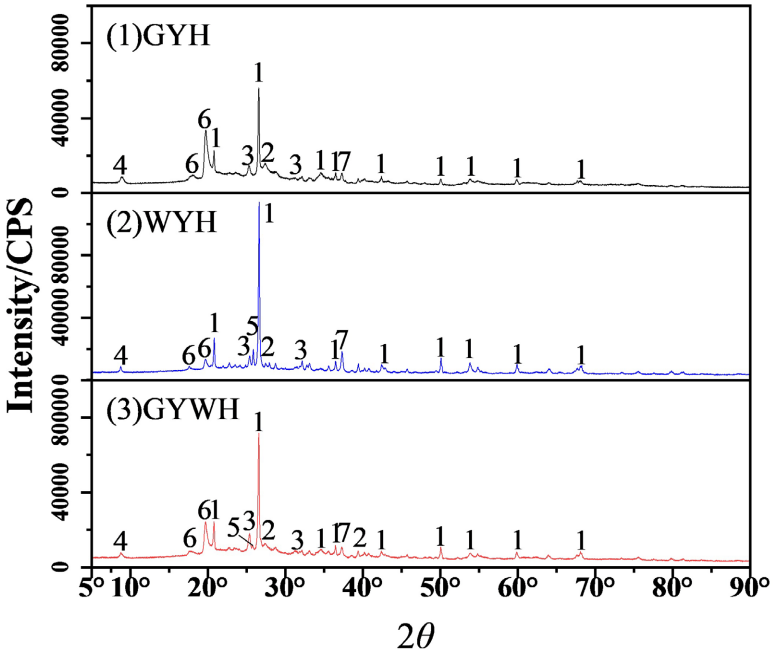

Note: 1-quartz; 2-anorthite; 3-anhydrite; 4-residual kaolinite; 5-mullite; 6-illite; 7-hematite.

Figure 8. XRD patterns of the representative combustion ash samples.

The XRD patterns of the combustion ashes are shown in **Figure 8**. Relative to the raw coals, the mineral assemblages exhibit clear high-temperature transformation. Quartz remains largely preserved because of its high chemical stability. Kaolinite and illite undergo dehydration/dehydroxylation, with part of the transformed aluminosilicate material recrystallizing as mullite ($3Al_2O_3{\cdot}2SiO_2$) [34]; Calcite-derived CaO can react with sulfur-bearing species to form anhydrite ($CaSO_4$) and with Al_2O_3/SiO_2 released from clay-mineral transformation to form Ca-bearing aluminosilicates such as anorthite ($CaAl_2Si_2O_8$). These phase changes establish the mineralogical basis for interpreting differences in ash morphology and slagging tendency.

The ash-phase distributions are consistent with the mineralogical differences of the parent coals. GYH contains more Ca-bearing high-temperature phases, including anhydrite and anorthite, and correspondingly shows a greater tendency toward low-melting or glass-forming behavior. WYH retains a stronger aluminosilicate signature, with more quartz, residual clay-related phases, and mullite, consistent with a more refractory ash framework. GYWH contains the principal phases found in both individual-coal ashes, with no new independent diffraction peak across 5˚ - 90˚ (2θ). Its phase composition is therefore intermediate rather than qualitatively new. This finding supports the interpretation that co-combustion modifies the relative abundance and spatial interaction of mineral phases without producing a new dominant crystalline assemblage.

3.4.2. SEM-EDS Analysis

1) Raw coal samples

The SEM observations provide microstructural context for the XRD and kinetic results. Figure 9 shows that GY and WY differ in surface texture, mineral coverage, and visible pore accessibility. These features may affect diffusion distances for oxygen and volatile products, but the images do not directly measure transport rates.

GY is dominated by bright-coal regions and contains numerous inherent cracks and pores within an otherwise relatively compact matrix. This comparatively open structure provides shorter potential pathways for oxygen penetration and volatile escape [35], consistent with the lower ignition temperature of GY. The local EDS field for GY has the highest measured C signal (75.66 wt.%; Table 5), which is consistent with greater exposure of carbonaceous material at that selected surface but does not quantify bulk organic content. Calcite is observed locally within cracks, showing spatial association without establishing a catalytic rate contribution.

WY shows a contrasting morphology, with extensive platy mineral coverage and flocculent/layered surface features. Such coverage could increase the effective oxygen-diffusion distance and reduce direct access to the underlying carbonaceous matrix [36]. In the representative EDS field, the combined Si and Al signal is 6.54%, approximately 1.7 times the corresponding local value for GY, consistent with stronger clay-mineral coverage at the imaged location. Because no replicate EDS fields were quantified, this comparison is descriptive and cannot establish a bulk difference or a causal transport coefficient.

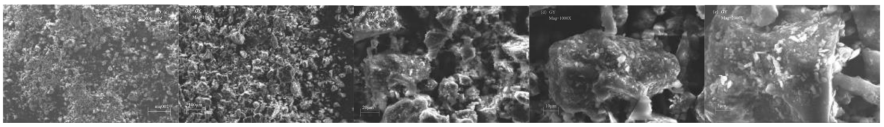

40 times 100 times 500 times 1000 times 2000 times

(a) GY

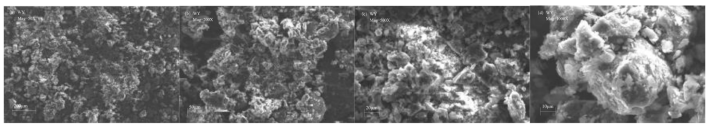

50 times 200 times 1000 times 2000 times

(b) WY

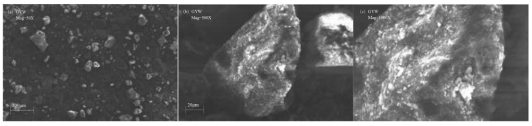

50 times 500 times 1000 times

(c) GYW

Figure 9. Representative SEM micrographs of the raw coal samples at different magnifications.

GYW contains both open-pore GY-like regions and clay-covered WY-like particles, providing a heterogeneous setting in which cross-component exchange could occur. The earlier ignition and devolatilization of GY while WY remains less converted create a temporal overlap consistent with such interaction. Radical transfer and pore-assisted oxygen transport are plausible pathways cited in the literature [37] [38], but neither radicals nor transport coefficients were measured here. The SEM observations therefore show structural conditions compatible with these hypotheses; they do not prove the pathways or quantify their contributions.

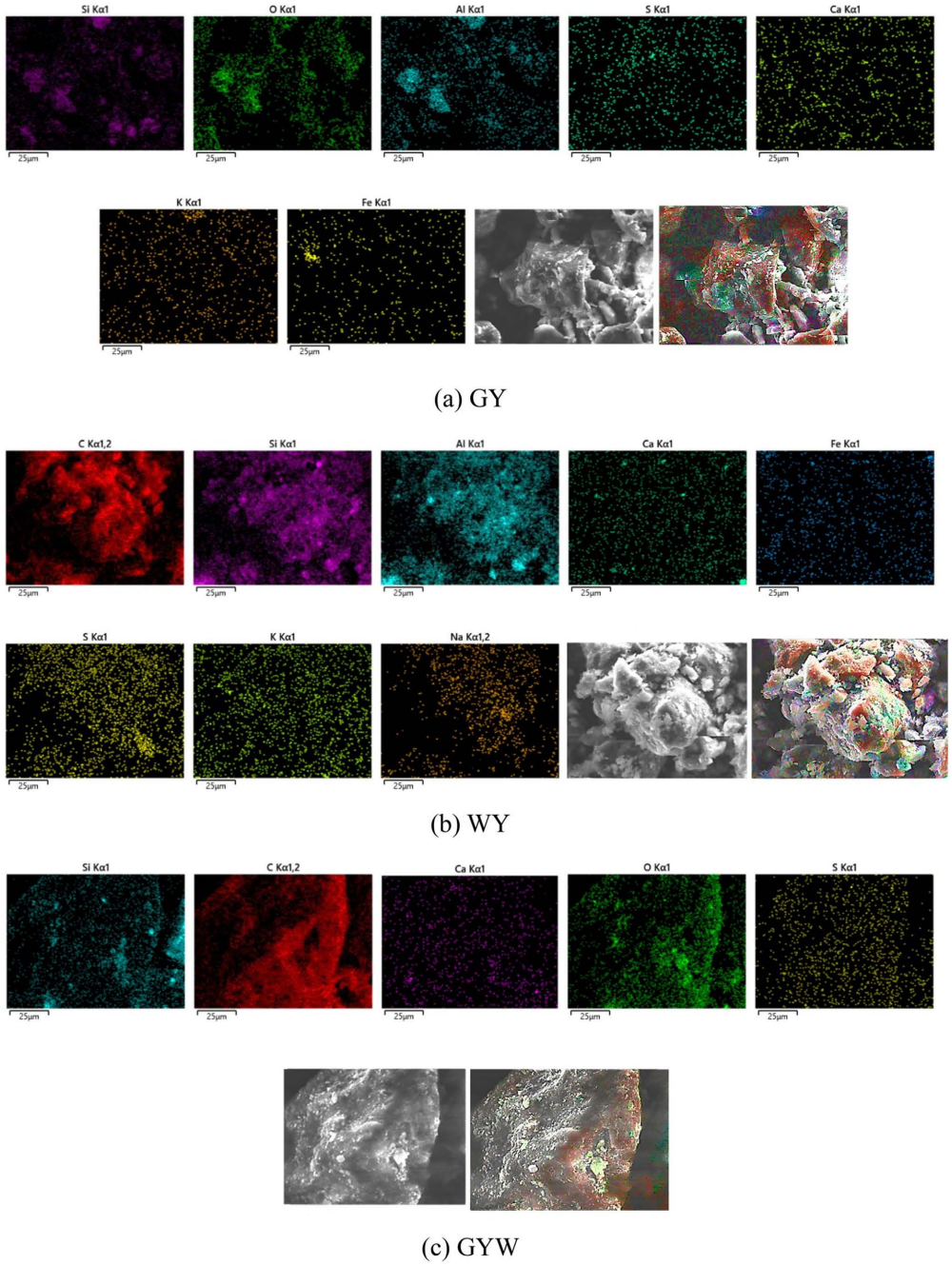

Figure 10. Representative SEM micrographs and EDS elemental maps of the raw coal samples.

The EDS elemental maps of representative raw-coal fields are shown in Figure 10, the corresponding spectra in Figure 11, and the local semi-quantitative compositions in Table 5**.** At the selected locations, C ranges from 70.01 to 75.66 wt.% and follows GY > GYW > WY, while O follows GYW > WY > GY. These local signals are consistent with different exposure of organic matter and oxygen-bearing minerals, but they should not be generalized as bulk compositions without replicated fields or an independent bulk assay.

At the representative locations, the higher O signals of WY and GYW are consistent with their oxygen-bearing mineral assemblages. Si and Al are spatially associated with quartz and clay minerals, while the selected GY field shows the highest local Ca signal (0.39%), consistent with calcite detected by XRD. Fe and S signals are similar and low at the analyzed locations. The agreement between EDS maps and XRD supports phase assignment at those locations, but EDS variability across particles was not quantified.

Table 5. Local semi-quantitative EDS composition of representative raw-coal fields.

Ultimate	GYH		WYH		GYWH	
	wt.%	At%	wt.%	At%	wt.%	At%
C	75.66	82.17	70.01	78.01	72.84	79.46
O	19.10	15.58	21.86	18.27	22.65	18.56
Na	\	\	0.16	0.09	\	\
Mg	\	\	\	\	0.13	0.07
Al	1.51	0.73	3.08	1.53	1.34	0.65
Si	2.32	1.08	3.46	1.65	2	0.93
S	0.27	0.11	0.32	0.13	0.19	0.08
K	0.26	0.09	0.25	0.09	0.14	0.05
Ca	0.39	0.13	0.27	0.09	0.26	0.09
Ti	\	\	0.11	0.03	\	\
Fe	0.49	0.11	0.44	0.11	0.45	0.11
Total	100	100	100	100	100	100

Overall, the raw-coal SEM-EDS observations are consistent with a proposed structure-reactivity relationship: the selected GY surfaces expose more open pores, whereas WY shows stronger mineral coverage. GYW contains both surface types. These observations provide morphological context for the TG-DTG results but do not independently quantify oxygen transport, radical transfer, or interparticle coupling.

The mineral and carbonaceous structures continue to evolve as combustion proceeds. SEM-EDS analysis of the combustion ashes was therefore used to describe post-combustion morphology and local elemental distributions. Because EDS is surface-sensitive and spatially local, it was not used as a bulk residual-carbon or burnout assay.

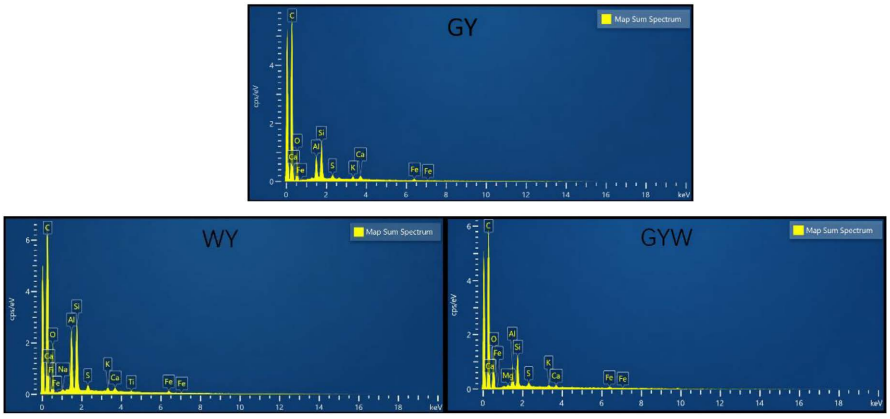

Figure 11. EDS spectra of the representative raw coal samples.

2) Combustion ash samples

Representative SEM images of the combustion ashes are shown in Figure 12. GYH and WYH exhibit markedly different morphologies over 50× - 5000×, consistent with their different mineral assemblages and slagging tendencies. GYH contains extensive glassy or partially fused regions, rounded particle edges, and local agglomeration. These features are consistent with the greater abundance of Ca-bearing transformation products identified by XRD and suggest a higher propensity for liquid-phase-assisted particle bonding.

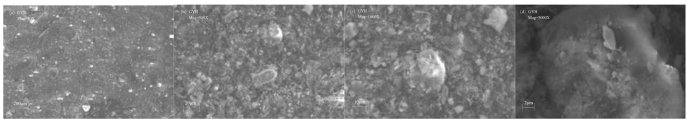

50 times 500 times 1000 times 5000 times

(a) GYH

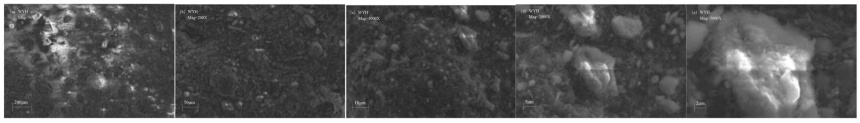

50 times 200 times 1000 times 2000 times 5000 times

(b) WYH

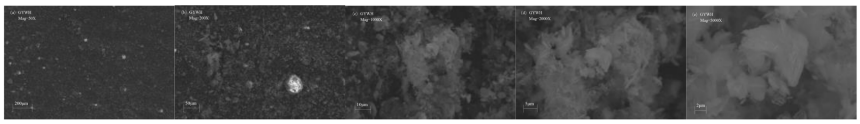

50 times 200 times 1000 times 2000 times 5000 times

(c) GYWH

Figure 12. Representative SEM micrographs of the combustion ash samples at different magnifications.

WYH is dominated by more discrete particles with limited evidence of liquid-phase bonding. Needle-like mullite and abundant fine pores produce a comparatively open ash structure. The representative WYH EDS field has a local C signal of 41.55 wt.% (Table 6). This value cannot be interpreted as a bulk residual-carbon

fraction because replicate positions and an independent bulk carbon measurement were not obtained; it only documents carbon detected in the selected surface field.

GYWH exhibits an intermediate morphology, containing both fused/agglomerated domains and discrete porous particles; mullite-rich features and glassy regions coexist at higher magnification. The representative local EDS C signals follow WYH (41.55 wt.%) > GYWH (30.86 wt.%) > GYH (12.67 wt.%) at the selected fields. This ordering is not used as quantitative evidence of bulk burnout or residual-carbon fractions. It may reflect true local residual carbon, particle-to-particle heterogeneity, mounting contributions, or a combination of these effects.

Figure 13 presents EDS elemental maps of representative combustion-ash fields, Figure 14 shows the corresponding spectra, and Table 6 summarizes the local semi-quantitative compositions.

Table 6. Local semi-quantitative EDS composition of representative combustion-ash fields.

Ultimate	GYH		WYH		GYWH	
	wt.%	At%	wt.%	At%	wt.%	At%
C	12.67	19.12	41.55	52.55	30.86	41.29
O	51.44	58.26	41.87	39.76	45.63	45.83
Na	0.79	0.62	0.17	0.11	0.43	0.30
Mg	0.36	0.27	0.29	0.18	0.23	0.15
Al	13.9	9.34	5.19	2.33	8.71	5.19
Si	15.94	10.29	7.04	3.76	10.21	5.84
P	0.25	0.15	\	\	0.14	0.07
S	0.29	0.16	0.30	0.14	0.39	0.19
K	0.92	0.43	0.48	0.18	0.58	0.24
Ca	1.52	0.69	1.37	0.51	1.25	0.50
Ti	0.73	0.28	0.29	0.09	0.40	0.13
Fe	1.19	0.39	1.45	0.39	0.77	0.22
Ba	\	\	\	\	0.40	0.05
Total	100	100	100	100	100	100

At the representative fields, several major-element signals for GYWH fall between those measured for GYH and WYH, consistent with mixed mineralogical features observed by XRD. Oxygen and the fluxing-element signals vary among the selected fields, while spatial maps show Ca-rich regions in GYH and interwoven Si-Al domains in WYH. These local patterns help interpret the imaged particles but do not establish bulk ash composition, bulk residual-carbon ordering, or statistical differences among samples. The Ba signal detected only in the selected GYWH field is therefore treated as local trace-element heterogeneity rather than evidence of a blend-specific phase.

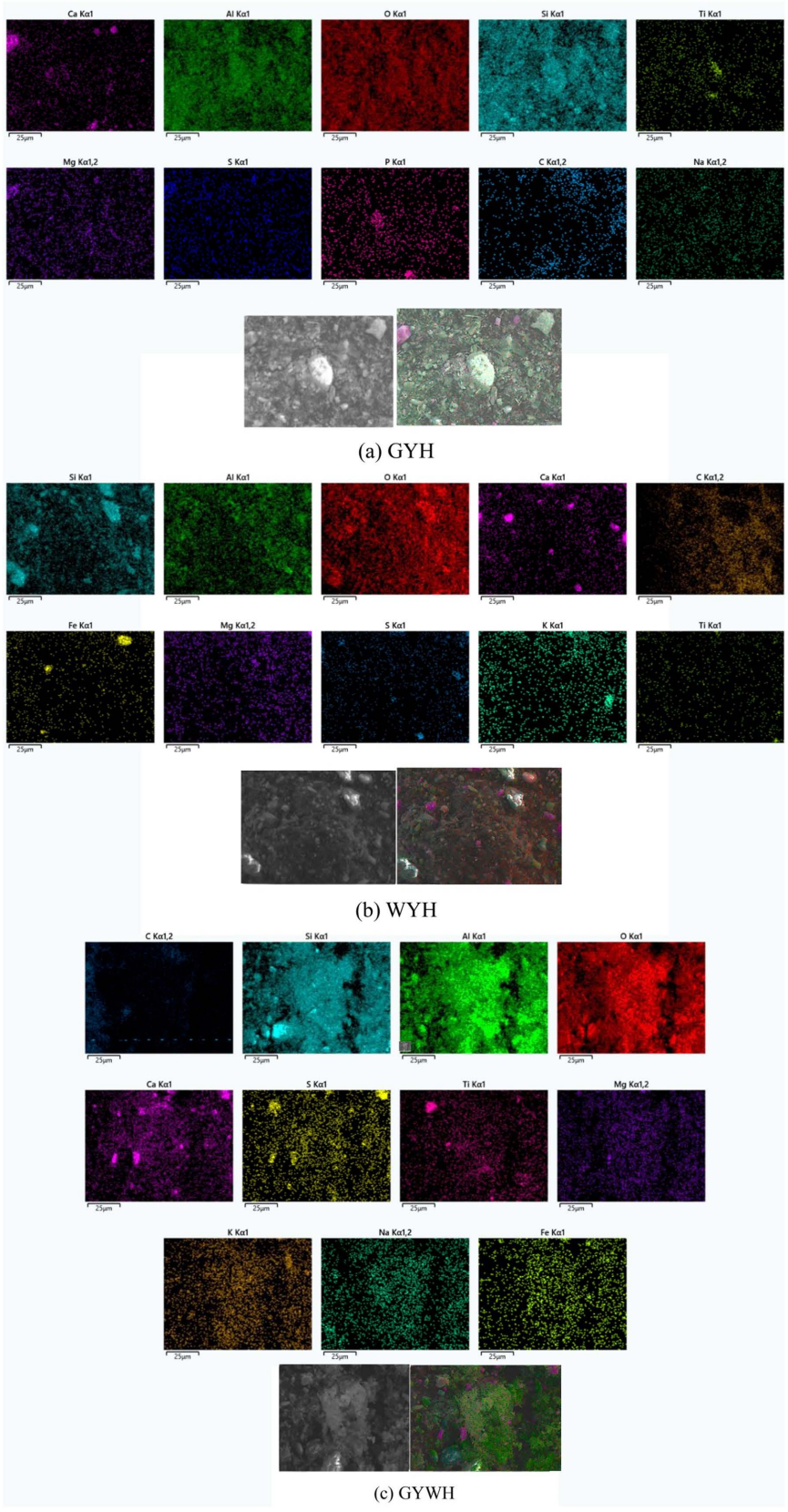

Figure 13. Representative SEM micrographs and EDS elemental maps of the combustion ash samples.

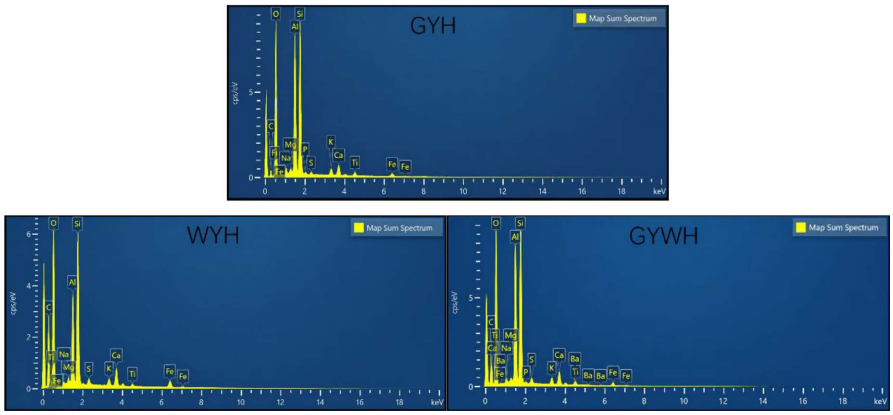

Figure 14. EDS spectra of the representative combustion ash samples.

4. Conclusions

By integrating TG-DTG behavior, a mass-weighted non-additivity analysis, model-free isoconversional kinetics, XRD, and SEM-EDS, this study provides an evidence-bounded description of GY/WY co-combustion. The principal conclusions are as follows:

1) GY and WY exhibit different combustion-temperature windows. At 10˚C/min, GY ignites at 294.12˚C, whereas WY ignites at 412.95˚C and burns out at 616.87˚C. These differences are consistent with the higher volatile content of GY and the low volatile content and condensed carbon structure of WY. GYW is intermediate; its earlier ignition than WY is expected from the GY fraction and is not, by itself, evidence that the intrinsic WY barrier is reduced.

2) Increasing the heating rate from 5˚C to 20˚C/min shifts TG-DTG features toward higher temperatures and increases peak mass-loss rates. The S index increases monotonically, whereas C decreases from 5˚C to 10˚C/min and only partially recovers at 20˚C/min. Faster heating therefore produces thermal lag and a higher instantaneous rate, not a uniform improvement in all combustion indices.

3) GYW shows small sign-changing deviations from the mass-weighted reference. Under $\Delta w = TG_{\text{exp}} - TG_{\text{cal}}$, negative Δw represents apparent promotion and positive Δw apparent inhibition. At 10˚C/min, −0.739% near 528˚C is the largest apparent promotion and +0.981% near 590˚C is apparent inhibition. Across the reported conditions, deviations of 0.22% - 1.65% remain within the <2% reproducibility screen; with n = 2, they are descriptive non-additivity and not statistically resolved synergy.

4) The three isoconversional methods give similar conversion-dependent Eα profile shapes with $R^2 > 0.98$. At the same conversion, GYW generally lies between GY and WY and is not systematically below WY. The kinetic results therefore do not demonstrate that blending lowers the intrinsic activation-energy barrier of WY. The approximately 128 kJ/mol average reported for GYW and any quoted spread across methods describe method-to-method estimates, not replicate uncertainty.

5) XRD directly identifies clay-rich WY, more evident Ca-bearing phases in GY,

and no new dominant crystalline phase in GYW; SEM directly documents differences in surface coverage and pore morphology. EDS values are local semi-quantitative signals and cannot be interpreted as bulk residual-carbon fractions. Heat transfer, radical exchange, pore evolution, and Ca/AAEM-mediated effects remain plausible explanations that require pathway-specific measurements for causal confirmation.

Overall, the measured results establish rank-dependent combustion, kinetic, mineralogical, and morphological differences and small deviations of the blend from an additive TG reference. A multiscale interaction framework is offered as a hypothesis consistent with these observations, not as a set of experimentally proven causal pathways. This distinction preserves the practical relevance of the results while matching the strength of the available evidence.

Funding

This work was supported by the CR Power Theory R&D Program (Grant No. CRP-R&D-LX-2025-031).

Data Availability Statement

All relevant data are within the paper.

Acknowledgements

This work was supported by the CR Power Theory R&D Program.

Author Contributions

Conceptualization, Zhu Cui; methodology, Zhu Cui; software, Yangyang Ma; validation, Jiahui Zhao; formal analysis, Yangyang Ma; investigation, Jiahui Zhao and Dazhuang Liu; resources, Jiahui Zhao and Dazhuang Liu; data curation, Zhu Cui; writing-original draft preparation, Zhu Cui; writing-review and editing, Zhu Cui; visualization, Xin Zhang; supervision, Xin Zhang; project administration, Zhu Cui; funding acquisition, Yangyang Ma. All authors have read and agreed to the published version of the manuscript.

Conflicts of Interest

The authors declare no conflict of interest.

References

[1] Syrodoy, S.V., Kostoreva, J.A., Kostoreva, A.A. and Asadullina, L.I. (2020) Ignition of Wood and Coal Particle Mixtures in Conditions of Steam and Water Boiler Furnaces. *Journal of the Energy Institute*, **93**, 443-449. https://doi.org/10.1016/j.joei.2019.07.007

[2] Peralta, D., Paterson, N.P., Dugwell, D.R. and Kandiyoti, R. (2001) Coal Blend Performance during Pulverised-Fuel Combustion: Estimation of Relative Reactivities by a Bomb-Calorimeter Test. *Fuel*, **80**, 1623-1634. https://doi.org/10.1016/s0016-2361(01)00031-x

[3] Gao, Q., Li, S., Xu, Y. and Liu, J. (2019) A General Mechanistic Model of Fly Ash Formation during Pulverized Coal Combustion. *Combustion and Flame*, **200**, 374-386. https://doi.org/10.1016/j.combustflame.2018.11.022

[4] Zhan, Z., Fry, A., Zhang, Y. and Wendt, J.O.L. (2015) Ash Aerosol Formation from Oxy-Coal Combustion and Its Relation to Ash Deposit Chemistry. *Proceedings of the Combustion Institute*, **35**, 2373-2380. https://doi.org/10.1016/j.proci.2014.07.001

[5] Su, S., Pohl, J.H., Holcombe, D. and Hart, J.A. (2001) Techniques to Determine Ignition, Flame Stability and Burnout of Blended Coals in P.F. Power Station Boilers. *Progress in Energy and Combustion Science*, **27**, 75-98. https://doi.org/10.1016/s0360-1285(00)00006-x

[6] Yang, X., Tong, C., Chen, G., Zhang, Y. and Jin, B. (2023) An Investigation of Pore Structure of Blended Coal Coke Produced by Pyrolysis of Three Kinds of Coal. *International Journal of Coal Preparation and Utilization*, **43**, 922-950. https://doi.org/10.1080/19392699.2022.2089126

[7] Zhang, Z., Li, Z. and Cai, N. (2016) Formation of Reductive and Corrosive Gases during Air-Staged Combustion of Blends of Anthracite/Sub-Bituminous Coals. *Energy & Fuels*, **30**, 4353-4362. https://doi.org/10.1021/acs.energyfuels.6b00599

[8] Yang, X., Chen, G., Huang, L., Gu, S., Li, C., Zhang, Y., *et al.* (2021) Experimental Study on Bituminous Coal Blending in a Down-Fired Boiler with Anthracite Combustion System under Low Load. *Asia-Pacific Journal of Chemical Engineering*, **16**, e2676. https://doi.org/10.1002/apj.2676

[9] Tong, C., Yang, X., Chen, G., Zhang, Y., Chen, L., Zhou, Y., *et al.* (2021) Experimental Investigation for the Combustion Characteristics of Blends of Three Kinds of Coal. *Fuel*, **300**, Article ID: 120937. https://doi.org/10.1016/j.fuel.2021.120937

[10] Wang, C., Liu, Y., Zhang, X. and Che, D. (2011) A Study on Coal Properties and Combustion Characteristics of Blended Coals in Northwestern China. *Energy & Fuels*, **25**, 3634-3645. https://doi.org/10.1021/ef200686d

[11] Ma, L., Guo, A., Fang, Q., Wang, T., Zhang, C. and Chen, G. (2018) Combustion Interactions of Blended Coals in an O_2/CO_2 Mixture in a Drop-Tube Furnace: Experimental Investigation and Numerical Simulation. *Applied Thermal Engineering*, **145**, 184-200. https://doi.org/10.1016/j.applthermaleng.2018.09.033

[12] Casal, M.D., Vega, M.F., Diaz-Faes, E. and Barriocanal, C. (2018) The Influence of Chemical Structure on the Kinetics of Coal Pyrolysis. *International Journal of Coal Geology*, **195**, 415-422. https://doi.org/10.1016/j.coal.2018.06.014

[13] Li, L., Tahmasebi, A., Dou, J., Lee, S., Li, L. and Yu, J. (2020) Influence of Functional Group Structures on Combustion Behavior of Pulverized Coal Particles. *Journal of the Energy Institute*, **93**, 2124-2132. https://doi.org/10.1016/j.joei.2020.05.007

[14] Vassilev, S.V. and Vassileva, C.G. (2009) A New Approach for the Combined Chemical and Mineral Classification of the Inorganic Matter in Coal. 1. Chemical and Mineral Classification Systems. *Fuel*, **88**, 235-245. https://doi.org/10.1016/j.fuel.2008.09.006

[15] Qin, S., He, X., Li, Z., Jia, L., Qiao, X., Chang, X., *et al.* (2025) Co-Combustion of Sewage Sludge and High Ash Coal: Thermal Behavior, Ash Formation Behavior, Interaction Mechanisms and Economic Analysis. *Energy*, **323**, Article ID: 135847. https://doi.org/10.1016/j.energy.2025.135847

[16] Mureddu, M., Dessì, F., Orsini, A., Ferrara, F. and Pettinau, A. (2018) Air- and Oxygen-Blown Characterization of Coal and Biomass by Thermogravimetric Analysis. *Fuel*, **212**, 626-637. https://doi.org/10.1016/j.fuel.2017.10.005

[17] Wu, C., Li, J., Shi, B. and Xue, Y. (2026) Experimental Study on Thermal Decompo-

sition and Kinetic Characteristics of Coal in $O_2/CO_2/N_2$ Atmospheres with Various CO_2/N_2 Blend Ratios. *Case Studies in Thermal Engineering*, **78**, Article ID: 107653. https://doi.org/10.1016/j.csite.2026.107653

[18] Chen, Z., Li, J., Zhang, X., Qiao, Y., Yuan, Z. and Li, Z. (2022) Investigation on Thermal Conversion, Kinetics and Thermodynamics of Coal Gasification Filter Cake Ash in Oxygen Fuel Combustion. *Fuel*, **330**, Article ID: 125556. https://doi.org/10.1016/j.fuel.2022.125556

[19] Vyazovkin, S., Burnham, A.K., Criado, J.M., Pérez-Maqueda, L.A., Popescu, C. and Sbirrazzuoli, N. (2011) ICTAC Kinetics Committee Recommendations for Performing Kinetic Computations on Thermal Analysis Data. *Thermochimica Acta*, **520**, 1-19. https://doi.org/10.1016/j.tca.2011.03.034

[20] Sharma, A., Aravind Kumar, A., Mohanty, B. and Sawarkar, A.N. (2023) Critical Insights into Pyrolysis and Co-Pyrolysis of Poplar and Eucalyptus Wood Sawdust: Physico-Chemical Characterization, Kinetic Triplets, Reaction Mechanism, and Thermodynamic Analysis. *Renewable Energy*, **210**, 321-334. https://doi.org/10.1016/j.renene.2023.04.066

[21] Cao, Y., Chen, Z., Boukhir, M., Dong, B., Zhang, J., Gu, S., *et al.* (2024) Insight into the Pyrolysis of Bamboo Flour, Polylactic Acid and Their Composite: Pyrolysis Behavior, Kinetic Triplets, and Thermodynamic Parameters Based on Fraser-Suzuki Deconvolution Procedure. *Bioresource Technology*, **391**, Article ID: 129932. https://doi.org/10.1016/j.biortech.2023.129932

[22] Chen, Y., Li, D., Tian, Y., Shi, J., Wen, D., Zhang, Y., *et al.* (2025) Non-Isothermal Co-Combustion of Sludge and Coal: Thermal Behavior, Kinetics and Functional Group Structural Analysis. *Energy*, **324**, Article ID: 135977. https://doi.org/10.1016/j.energy.2025.135977

[23] Meng, D., Yue, C., Wang, T. and Chen, X. (2021) Evolution of Carbon Structure and Functional Group during Shenmu Lump Coal Pyrolysis. *Fuel*, **287**, Article ID: 119538. https://doi.org/10.1016/j.fuel.2020.119538

[24] Kong, L., Li, G., Jin, L. and Hu, H. (2015) Pyrolysis Behaviors of Two Coal-Related Model Compounds on a Fixed-Bed Reactor. *Fuel Processing Technology*, **129**, 113-119. https://doi.org/10.1016/j.fuproc.2014.09.009

[25] Haykiri-Acma, H. and Yaman, S. (2010) Interaction between Biomass and Different Rank Coals during Co-Pyrolysis. *Renewable Energy*, **35**, 288-292. https://doi.org/10.1016/j.renene.2009.08.001

[26] Zhao, D., Liu, H., Zhu, D. and Qin, M. (2020) Effect of O-Containing Functional Groups Produced by Preoxidation on Zhundong Coal Gasification. *Fuel Processing Technology*, **206**, Article ID: 106480. https://doi.org/10.1016/j.fuproc.2020.106480

[27] Chen, H., Wang, F., Zhang, D., Deng, H., Wen, X. and Chen, G. (2025) Kinetic and Thermodynamic Analysis of Synergistic Pyrolysis of Salix Psammophila and Plastic Waste. *Thermochimica Acta*, **751**, Article ID: 180060. https://doi.org/10.1016/j.tca.2025.180060

[28] Wang, R., Liu, Z., Song, X. and Liu, S. (2023) Co-Combustion of Pulverized Coal and Walnut Shells in Air and Oxy-Fuel Atmospheres: Thermal Behavior, Synergistic Effect and Kinetics. *Journal of the Energy Institute*, **108**, Article ID: 101243. https://doi.org/10.1016/j.joei.2023.101243

[29] Feng, W.G, Lou, G.F. and Wang, G. (2017) Experimental Study on the Kinetics of Coke Combustion under Different Atmospheres. *Chemical Progress*, **36**, 487-493.

[30] Gan, X., Chen, Z., Ma, W., Zhang, Y., Qu, J., Han, C., *et al.* (2026) Kinetic and Thermodynamic Analyses of Multigranular Low-Rank Coal: Synergistic Effect of Particle

Size on Reactivity and Coke Properties. *Fuel*, **406**, Article ID: 137065. https://doi.org/10.1016/j.fuel.2025.137065

[31] Zhang, L., Hower, J.C. and Liu, W. (2016) Devolatilization and Kinetics of Maceral Concentrates of Bituminous Coals. *Fuel Processing Technology*, **154**, 147-155. https://doi.org/10.1016/j.fuproc.2016.08.026

[32] Zhou, H., Wu, C., Pan, J., Wang, Z., Niu, Q. and Du, M. (2021) Research on Molecular Structure Characteristics of Vitrinite and Inertinite from Bituminous Coal with FTIR, Micro-Raman, and XRD Spectroscopy. *Energy & Fuels*, **35**, 1322-1335. https://doi.org/10.1021/acs.energyfuels.0c03586

[33] Zhang, L., Liu, W. and Men, D. (2014) Preparation and Coking Properties of Coal Maceral Concentrates. *International Journal of Mining Science and Technology*, **24**, 93-98. https://doi.org/10.1016/j.ijmst.2013.12.016

[34] Lei, T., Zhao, J. and Zhang, Z. (2024) *In-Situ* Ash Sintering Process Analysis during the Co-Combustion of the Coal Gasification Fine Slag and Corn Straw. *Energy*, **310**, Article ID: 133311. https://doi.org/10.1016/j.energy.2024.133311

[35] Cheng, J., Zhang, Y., Wang, T., Norris, P., Chen, W. and Pan, W. (2017) Thermogravimetric-Fourier Transform Infrared Spectroscopy-Gas Chromatography/Mass Spectrometry Study of Volatile Organic Compounds from Coal Pyrolysis. *Energy & Fuels*, **31**, 7042-7051. https://doi.org/10.1021/acs.energyfuels.7b01073

[36] Wu, Q., Wu, N., Wang, Z., Ding, L., Wang, C., Chen, J., *et al.* (2026) Experimental Investigation on Ammonia/Coal Co-Firing of Zhundong Coal and Anthracite: A Comparative Study of Combustion Performance, Fuel-N Conversion and Ash Deposition. *Journal of the Energy Institute*, **125**, Article ID: 102471. https://doi.org/10.1016/j.joei.2026.102471

[37] Han, F., Meng, A., Li, Q. and Zhang, Y. (2016) Thermal Decomposition and Evolved Gas Analysis (TG-MS) of Lignite Coals from Southwest China. *Journal of the Energy Institute*, **89**, 94-100. https://doi.org/10.1016/j.joei.2015.01.007

[38] Chen, C., Wang, Z., Zhu, R., Tan, J., He, Y. and Cen, K. (2023) Co-Firing Characteristics and Fuel-N Transformation of Ammonia/Pulverized Coal Binary Fuel. *Fuel*, **337**, Article ID: 126857. https://doi.org/10.1016/j.fuel.2022.126857